

# Möbius Insulator and Higher-Order Topology in $\text{MnBi}_{2n}\text{Te}_{3n+1}$

Rui-Xing Zhang,<sup>1,\*</sup> Fengcheng Wu,<sup>1,†</sup> and S. Das Sarma<sup>1</sup>

<sup>1</sup>*Condensed Matter Theory Center and Joint Quantum Institute, Department of Physics,  
University of Maryland, College Park, Maryland 20742-4111, USA*

(Dated: September 2, 2022)

We propose  $\text{MnBi}_{2n}\text{Te}_{3n+1}$  as a magnetically tunable platform for realizing various symmetry-protected higher-order topology. Its canted antiferromagnetic phase can host exotic topological surface states with a Möbius twist that are protected by nonsymmorphic symmetry. Moreover, opposite surfaces hosting Möbius fermions are connected by one-dimensional chiral hinge modes, which offers the *first* material candidate of a higher-order topological Möbius insulator. We uncover a general mechanism to feasibly induce this exotic physics by applying a small in-plane magnetic field to the antiferromagnetic topological insulating phase of  $\text{MnBi}_{2n}\text{Te}_{3n+1}$ , as well as other proposed axion insulators. For other magnetic configurations, two classes of inversion-protected higher-order topological phases are ubiquitous in this system, which both manifest gapped surfaces and gapless chiral hinge modes. We systematically discuss their classification, microscopic mechanisms, and experimental signatures. Remarkably, the magnetic-field-induced transition between distinct chiral hinge mode configurations provides an effective “topological magnetic switch”.

*Introduction* - The past decade has witnessed the rapid development of topological crystalline insulators (TCI) as a new class of materials [1–10], where crystalline group symmetries protect band topology in solids. The bulk topology of a TCI enforces protected in-gap states to emerge only on its symmetry-preserving boundaries. Recently, it was realized that a special class of TCI also features higher-order topology [11–17], where gapless modes live on  $(D-d)$ -dimensional boundary of a  $D$ -dimensional TCI with  $1 < d \leq D$ . Theoretical work on these higher-order topological insulators (HOTI) has mainly focused on topological classifications and model constructions, with only a few realistic candidate materials being proposed [18–21]. Experimentally, the only evidence for electronic HOTI was demonstrated in bismuth [18]. Therefore, identifying more experimentally accessible HOTI systems is important.

Recently, a major breakthrough for TCI is the discovery of antiferromagnetic (AFM) topological insulators (TI) in  $\text{MnBi}_{2n}\text{Te}_{3n+1}$  family of materials [22–31]. With intrinsic  $A$ -type AFM order and an out-of-plane easy axis, the band topology of  $\text{MnBi}_{2n}\text{Te}_{3n+1}$  is protected by an AFM time-reversal symmetry (TRS)  $\Theta_M$ , which combines the TRS operation  $\Theta$  and a half-unit-cell translation  $T_{[00\frac{1}{2}]}$  along  $\hat{z}$  direction. Compounds with  $n = 1, 2, 3$  (i.e.,  $\text{MnBi}_2\text{Te}_4$ ,  $\text{MnBi}_4\text{Te}_7$ , and  $\text{MnBi}_6\text{Te}_{10}$ ) are currently under active experimental study [27, 28, 32–37]. Remarkably, evidence of quantum anomalous Hall effect [38, 39] and axion insulator [40] has recently been reported in few-layer  $\text{MnBi}_2\text{Te}_4$ . Since the magnetic moments of  $\text{MnBi}_{2n}\text{Te}_{3n+1}$  can be easily manipulated by a weak applied magnetic field, it is an interesting open question on the type of band topology that could arise for various field-induced magnetic configurations in  $\text{MnBi}_{2n}\text{Te}_{3n+1}$ .

In this Letter, we propose  $\text{MnBi}_{2n}\text{Te}_{3n+1}$  as a highly tunable system to realize a variety of HOTI phases. In particular, we show that applying an in-plane field cants the AFM ordering and leads to the *first* material platform for a higher-order Möbius insulator with a Möbius twist in its topological surface state, as schematically shown in Fig. 1. Furthermore, opposite surfaces hosting Möbius states are connected by 1d chiral hinge modes, manifesting the higher-order nature. For general magnetic configurations, two distinct classes of inversion-protected HOTIs are expected in  $\text{MnBi}_{2n}\text{Te}_{3n+1}$ . These two HOTI phases share the same bulk topological index but differ in their hinge mode configurations. Rotating the magnetic field can drive transition between these two phases, and therefore, can lead to a topological magnetic switching of  $G_{zz}$ , the two-terminal conductance along  $\hat{z}$  direction. We also discuss experimental consequences and application of our theory to other proposed axion insulators.

*Model Hamiltonian* - We start by defining an effective Hamiltonian for  $\text{MnBi}_{2n}\text{Te}_{3n+1}$  that captures its essential symmetry and topological features. In the absence of magnetism, the point group of  $\text{MnBi}_{2n}\text{Te}_{3n+1}$  is  $D_{3d}$ , which can be generated by (i) a three-fold rotation  $C_{3z}$  around  $z$ -axis, (ii) a two-fold rotation  $C_{2x}$  around  $x$ -axis, and (iii) the spatial inversion  $\mathcal{I}$ .  $D_{3d}$  also contains three in-plane mirror operations including  $M_x$ . Following earlier first-principles calculations [22, 32], we consider the basis functions  $|\uparrow(\downarrow, \pm)\rangle$  with  $\pm$  parity eigenvalues. This defines a four-band  $\mathbf{k} \cdot \mathbf{p}$  Hamiltonian  $H_0(\mathbf{k})$  around  $\Gamma$  point, which resembles that for  $\text{Bi}_2\text{Se}_3$  [41] and describes a 3d massive Dirac fermion. In particular,  $H_0(\mathbf{k}) = e(\mathbf{k})\mathbb{I}_4 + \sum_{i=1}^5 d_i(\mathbf{k})\Gamma_i$ , where  $\mathbb{I}_4$  is the identity matrix,  $\Gamma_i = s_i \otimes \sigma_1$  for  $i = 1, 2, 3$ ,  $\Gamma_4 = s_0 \otimes \sigma_2$ , and  $\Gamma_5 = s_0 \otimes \sigma_3$ .  $s_i$  and  $\sigma_i$  are the Pauli matrices for the spin and orbital degrees of freedom, respectively. The point group symmetry constrains the explicit forms of  $d_i(\mathbf{k})$  to be  $d_1 = vk_x$ ,  $d_2 = vk_y$ ,  $d_3 = v_z k_z$ ,  $d_4 = w(k_+^3 + k_-^3)$ ,  $d_5 = M_0 + M_1 k_z^2 + M_2(k_x^2 + k_y^2)$ , and  $e(\mathbf{k}) = C_0 + C_1 k_z^2 + C_2(k_x^2 + k_y^2)$ . Physically,  $v$  and  $v_z$  de-

\* ruixing@umd.edu

† wufcheng@umd.edu

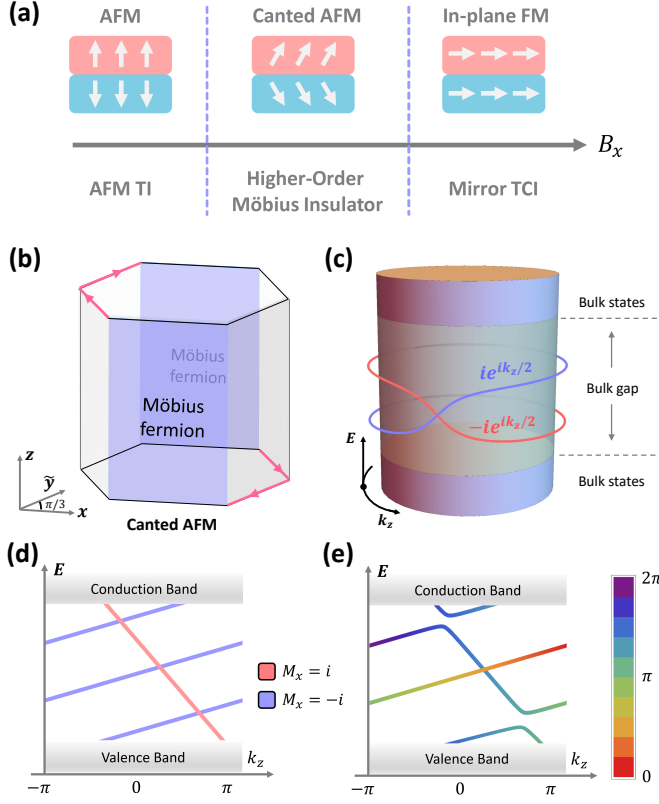


FIG. 1. (a) Applying an in-plane field  $B_x$  to an AFM TI induces a topological transition to a higher-order Möbius insulator, and eventually to a mirror TCI protected by  $M_x$ . (b) Schematic of a higher-order Möbius insulator in a hexagonal geometry. The red arrows represent chiral hinge modes. (c) Schematic of surface Möbius fermions along the glide-invariant line (GIL) labeled with a  $\mathcal{G}_x$  eigenvalue of  $\pm ie^{ik_z/2}$ . Along GIL, the Möbius fermions can be disconnected from other bands. We schematically show how the surface state of a mirror TCI in (d) evolves into a Möbius fermion in (e), when the mirror symmetry is broken to  $\mathcal{G}_x$ . The color bar in (e) shows the phase of the corresponding  $\mathcal{G}_x$  eigenvalue. A gap opens when two surface states with the same color cross.

note the in-plane and out-of-plane Fermi velocities, while  $w$  controls the hexagonal warping effect and reduces the full rotation symmetry down to  $C_{3z}$ . For our purpose, we regularize our model on a 3d hexagonal lattice as shown in Fig. 2 (a). The full expression for the lattice model is given in the Supplemental Material (SM).

The pristine  $\text{MnBi}_{2n}\text{Te}_{3n+1}$  compounds usually develop A-type AFM ordering along (001) direction, as shown in Fig. 2 (a), where we introduce a sublayer index  $i = A, B$  to describe the AFM-induced unit cell doubling. We characterize the magnetization in sublayer  $i$  by  $\mathbf{M}_i = (\cos \phi_i \sin \theta_i, \sin \phi_i \sin \theta_i, \cos \theta_i)$  with angles  $\phi_i$  and  $\theta_i$ . In particular, the exchange coupling term is

$$H_{\text{ex}} = \begin{pmatrix} \mathbf{M}_A \cdot \vec{s} \otimes \sigma_0 & 0 \\ 0 & \mathbf{M}_B \cdot \vec{s} \otimes \sigma_0 \end{pmatrix}. \quad (1)$$

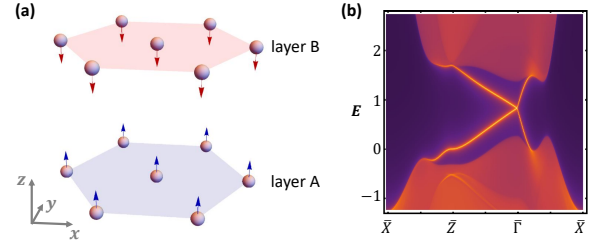


FIG. 2. (a) Lattice structure of our tight-binding model. (b) Surface spectrum for (010) surface of the AFM phase.

The AFM ordering is described by  $(\theta_A, \theta_B) = (0, \pi)$ . By choosing proper band parameters, we calculate the energy spectrum for the (010) surface of the AFM phase in a semi-infinite geometry using iterative Green function method. As shown in Fig. 2 (b), the system hosts a single gapless Dirac cone at  $\bar{\Gamma}$ , the origin of surface Brillouin zone (BZ). The gapless Dirac surface state here is protected by the AFM TRS  $\Theta_M$  and generally shows up for any surface that is compatible with  $\Theta_M$  symmetry [3]. On the other hand, a finite surface energy gap is expected on the (001) surface. The AFM TI phase serves as the starting point for our discussion on higher-order topology.

*Higher-Order Möbius Insulator* - In the presence of an external in-plane magnetic field  $\mathbf{B}$ , the AFM cant along the field direction [see Fig. 1 (a)] and generally breaks all symmetries except for the spatial inversion  $\mathcal{I}$ . The loss of  $\Theta_M$  generally leads to a magnetic surface gap for every surface and trivializes the  $\Theta_M$ -protected topology. However, this enables the possibility of higher-order topology emerging in this system.

When  $\mathbf{B}$  is along  $\hat{x}$  and hence perpendicular to the  $M_x$  mirror plane, the canted AFM ordering respects a non-symmorphic glide mirror symmetry  $\mathcal{G}_x$  that combines mirror reflection  $M_x$  and the half-unit-cell translation  $T_{[00\frac{1}{2}]}$  along  $\hat{z}$ , as shown in Fig. 3 (a). Along the glide-invariant line (GIL) of the nonsymmorphic 010 surface BZ (e.g.  $k_x = 0, \pi$ ), the surface states are labeled by their glide eigenvalues  $g_x = \pm ie^{ik_z/2}$ . Whenever surface states with distinct  $g_x$  cross, a “locally” robust surface Dirac point is formed. Nevertheless, only an odd number of surface Dirac points is *topologically robust* for this system, featuring  $\mathbb{Z}_2$  band topology [7, 8]. This motivates us to calculate the (010) surface spectrum for our canted AFM system. As shown in Fig. 3 (b), a single surface Dirac point is clearly revealed along GIL, which proves the topological nature of the canted AFM phase.

While the crystal momentum is  $2\pi$  periodic along GIL, the glide eigenvalue  $g_x$  follows a periodicity of  $4\pi$  due to the half-unit-cell translation. Therefore, the surface state manifold along GIL manifests itself as a Möbius twist for  $g_x$  [7, 9, 10], as schematically plotted in Fig. 1 (c). We thus dub this surface state as 2d “*Möbius fermions*”. Distinct from conventional surface states of topological insulators, the Möbius fermions can be disconnected from

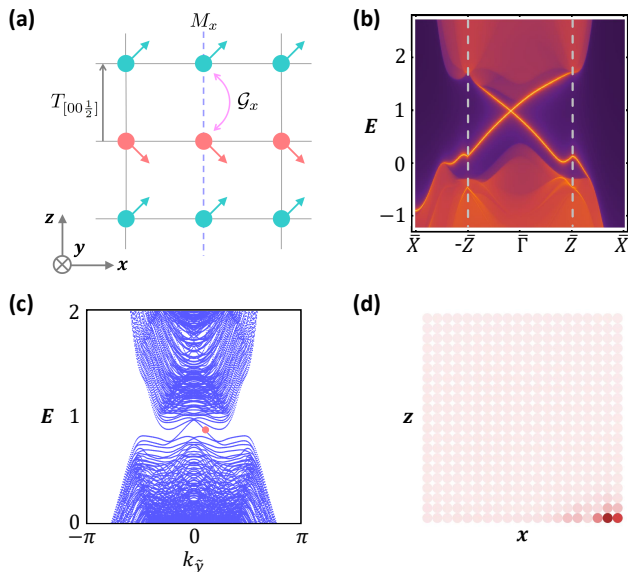


FIG. 3. (a) When magnetic moments in the canted AFM cant towards  $\hat{x}$  direction, the system has a glide mirror symmetry  $\mathcal{G}_x$ , which interchanges the green and red magnetic moments. (b) The surface spectrum on (010) surface for the canted AFM phase with  $\theta_A = \pi - \theta_B = 0.3\pi$  and  $\phi_A = \phi_B = 0$ . The glide-invariant line is sandwiched between two white dashed lines, where the Möbius fermion is well-defined. (c) The corresponding in-gap chiral hinge modes in a prism geometry periodic in  $\tilde{y}$  direction. (d) The real-space distribution in the  $x$ - $z$  plane for the chiral modes marked by the red dot in (c).

other surface or bulk bands along GIL, but are connected to higher-energy bands away from GIL for being unremovable. In our canted AFM phase, Möbius fermions only live on the (010) surfaces [i.e., the purple surfaces in Fig. 1 (b)] where glide symmetry is preserved, while surface gaps show up on all other surfaces.

Remarkably, there exist *hinge-localized 1d chiral modes* that connect those spatially disjoint surfaces with Möbius fermions, as shown in Fig. 1 (b). Indeed, while the glide symmetry  $\mathcal{G}_x$  allows for a  $\mathbb{Z}_2$  invariant  $\nu_g$  to characterize the Möbius fermions, a  $\mathbb{Z}_4$  symmetry indicator  $\kappa$  for the inversion symmetry  $\mathcal{I}$  can be simultaneously defined as [42]

$$\kappa \equiv \sum_{k_i} \frac{(n_+ - n_-)}{2} \pmod{4}. \quad (2)$$

Here  $n_{\pm}$  counts the number of occupied bands with  $\pm$  parity eigenvalues and the summation is over all inversion-symmetric crystal momenta. Physically, an odd  $\kappa$  implies a Weyl semimetal. When a system is known to be gapped, the  $\kappa = 2$  phase is an axion insulator with higher-order topology. Crucially, symmetry argument imposes a relation between  $\nu_g$  and  $\kappa$  as [43]

$$\nu_g \equiv \frac{\kappa}{2} \pmod{2}. \quad (3)$$

As a result, when Möbius fermions show up ( $\nu_g = 1$ ), the

chiral hinge mode is required to appear because of  $\kappa = 2$ , and vice versa.

A simple topological index analysis implies  $\kappa = 2$  in our model if the transition from AFM to canted AFM does NOT close the bulk gap. Numerically, we consider a prism geometry periodic along  $\tilde{y}$  with a finite cross section in its  $x$ - $z$  plane ( $20 \times 21$  lattice sites). Note that  $\tilde{y}$  differs from the Cartesian-coordinate  $\hat{y}$  axis by a  $\pi/6$  rotation around  $\hat{z}$ . Fig. 3 (c) plots the energy spectrum in this prism geometry, showing 1d chiral modes that traverse the surface gaps. In Fig. 3 (d), we depict the spatial profile of the left-moving mode in the  $x$ - $z$  cross section and find it localized at the bottom right corner, which verifies the hinge-mode picture. The existence of Möbius fermions on (010) surface and 1d chiral hinge modes along  $\tilde{y}$  direction together establishes our canted AFM phase as the only known realistic example of a “higher-order Möbius insulator”.

By gradually increasing the in-plane  $\mathbf{B}$  field, the canted AFM phase eventually evolves to an in-plane FM phase, which promotes the glide symmetry  $\mathcal{G}_x$  to a mirror symmetry  $M_x$ . As shown in Fig. 1 (a), the higher-order Möbius phase thus evolves to a mirror-protected TCI [2, 32] with no hinge physics. The transition from a Möbius fermion to a mirror-protected topological surface state is schematically shown in Figs. 1(d) and 1(e).

*Inversion-Protected Higher-Order Topology* - When  $\mathbf{B}$  deviates from  $\hat{x}$ , various new magnetic configurations can be induced that generally break the glide symmetry  $\mathcal{G}_x$  and thus spoil the Möbius physics, as well as the mirror TCI physics. Despite energy gaps on all surfaces because of lack of symmetries, the inversion indicator  $\kappa = 2$  remains well-defined as long as the bulk gap survives, which characterizes our system as a robust inversion-symmetric higher-order TI [15, 16] with chiral hinge mode. In particular, there exist two classes of inversion-symmetric HOTI phases in  $\text{MnBi}_{2n}\text{Te}_{3n+1}$ , which we discuss next.

When  $\text{MnBi}_{2n}\text{Te}_{3n+1}$  is ferromagnetic along  $\hat{z}$ , it realizes a HOTI that preserves three-fold rotation symmetry  $C_{3z}$ . When placed on a hexagonal geometry, the hinge mode configuration compatible with both inversion  $\mathcal{I}$  and  $C_{3z}$  is shown in Fig. 4 (c), which consists of three spatially separated chiral hinge modes along  $+\hat{z}$  along with their inversion partners on the opposite hinges. We call this phase the *HOTI  $\alpha$  phase* to distinguish it from the  $\beta$  phase defined later. Numerically, we calculate the energy spectrum of this out-of-plane ferromagnet in the hexagonal prism geometry with in-plane open boundary conditions and with periodicity in  $\hat{z}$  direction. As shown in Fig. 4 (a), we find three pairs of 1d modes that traverse the surface gap, which are further confirmed as chiral hinge modes by their spatial profiles plotted in Fig. 4 (b). These results together confirm the schematic in Fig. 4 (c).

In contrast, the *HOTI  $\beta$  phase* is defined by the chiral hinge mode trajectory shown in Fig. 4 (f), which explicitly breaks  $C_{3z}$  and has only one pair of chiral hinge modes along  $\hat{z}$ . The  $\beta$  phase can be induced by applying

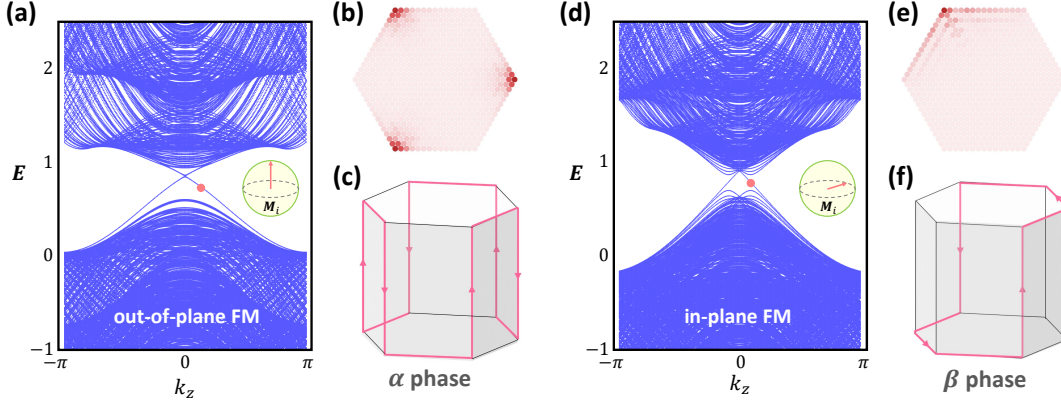


FIG. 4. (a) The hinge mode spectrum of the HOTI  $\alpha$  phase with  $\theta_A = \theta_B = 0$ . (b) The spatial profile of the left-moving hinge modes indicated by the red dot in (a), which confirms the schematic plot in (c). (d)-(f) Corresponding plots for the HOTI  $\beta$  phase.  $\phi_A = \phi_B = \frac{\pi}{6}$  and  $\theta_A = \theta_B = \frac{\pi}{2}$  for calculations done in (d) and (e).

a magnetic field off the high-symmetry directions, which holds for generic magnetic structures in  $\text{MnBi}_{2n}\text{Te}_{3n+1}$ . An example of  $\beta$  phase with FM ordering is numerically confirmed in Fig. 4 (d) and (e). In the SM, we provide a second example of  $\beta$  phase with canted AFM ordering. We emphasize that  $\alpha$  and  $\beta$  phases share the same bulk index  $\kappa = 2$  and are hence topologically equivalent. Although phenomenologically distinct, an  $\alpha$  phase can be transformed into a  $\beta$  phase by symmetrically attaching 2d layers of Chern insulator to the side surfaces. In other words,  $\alpha$  phase can be connected to  $\beta$  phase by *only* closing its surface gaps, which can be achieved by manipulating its bulk magnetic ordering via  $\mathbf{B}$  field.

*Experiment Signatures* - For a finite-slab geometry, the chiral hinge modes in both  $\alpha$  and  $\beta$  phases enable in-plane quantized anomalous Hall conductance  $\sigma_{xy} = e^2/h$ . Notably, this conductance quantization to  $e^2/h$  persists when the slab thickness grows, which signals 3d higher-order topology. In addition, we suggest using scanning tunneling microscopy to map out the in-gap local density of states (LDOS) on the top surface. As shown in Fig. 5 (a), we predict that for a HOTI  $\alpha$  phase, the LDOS on the top surface only peaks at some specific hinges or step edges. As a comparison, we also plot the in-gap LDOS peak of a 2d Chern insulator, which generally appears on all edges [Fig. 5 (b)]. This special LDOS pattern of the chiral hinge modes provides another direct experimental evidence for higher-order topology.

Meanwhile,  $\alpha$  and  $\beta$  phases behave distinctly in their out-of-plane transport measurements. In Fig. 5 (c), we propose measuring the two-terminal conductance  $G_{zz} = I_z/V_z$  by driving a  $\hat{z}$ -directional current  $I_z$  and measuring the voltage drop  $V_z$  between top and bottom surfaces. Although quantized signals are expected for both phases, the  $\alpha$  phase has  $G_{zz} = 3e^2/h$  while the  $\beta$  phase has  $G_{zz} = e^2/h$ . Since an in-plane magnetic field  $\mathbf{B}_{\parallel}$  generally drives the transition between these phases, this device realizes a “*topological magnetic switch*”, where the  $\mathbf{B}_{\parallel}$  controls a quantized jump of  $G_{zz}$  by a factor of 3 [Fig.

5 (c)]. Remarkably, the threshold for  $B_{\parallel}$  to trigger this switching could be as low as 0.2 T [27, 32], which holds promise for practical topological electronics.

*Conclusion* - We have proposed  $\text{MnBi}_{2n}\text{Te}_{3n+1}$  as a possible material class for realizing higher-order Möbius physics and various inversion-symmetric higher-order topological phases. For  $\text{MnBi}_2\text{Te}_4$ ,  $\text{MnBi}_4\text{Te}_7$ , and  $\text{MnBi}_6\text{Te}_{10}$ , A-type AFM physics have been reported at zero field and signatures of canted AFM have been observed with an in-plane magnetic field [24, 27, 28, 32, 33, 35]. Based on our topological index analysis, we expect those canted AFM systems to be exactly our proposed higher-order Möbius insulators, when the magnetic field is carefully aligned to preserve the glide symmetry.

For both  $\text{MnBi}_4\text{Te}_7$  and  $\text{MnBi}_6\text{Te}_{10}$ , an out-of-plane

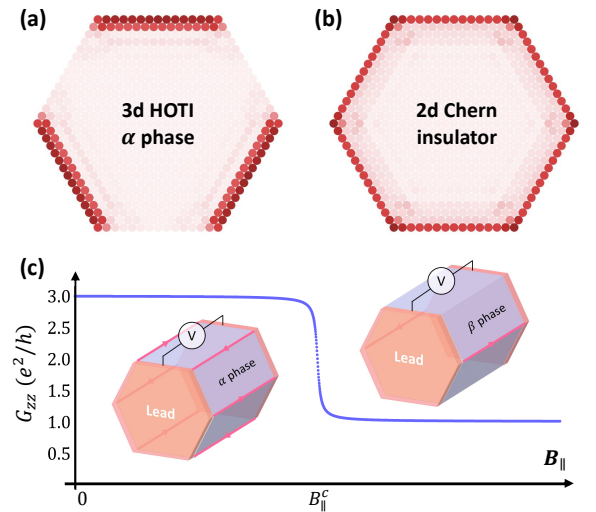


FIG. 5. In-gap LDOS for (a) the top surface of a HOTI  $\alpha$  phase and (b) a 2d Chern insulator. (c) The transition from HOTI  $\alpha$  phase to  $\beta$  phase is accompanied by a quantized jump in  $G_{zz}$ , which realizes a topological magnetic switch.

FM phase is observed at a small ( $\sim 0.2$  T) [27, 28, 32] or even vanishing field [33, 35]. Recent first-principles calculations suggest a non-trivial symmetry indicator  $\kappa = 2$  for the FM phases in both materials [32, 35], which supports our prediction of the HOTI  $\alpha$  phase in these FM systems. Moreover, the HOTI  $\beta$  phase and the topological magnetic switch effect can be feasibly achieved by simply rotating the magnetic field.

Finally, we emphasize that our theory provides a microscopic mechanism for higher-order Möbius insulators in magnetic topological materials. For example, the

higher-order Möbius physics can also be realized on the (010) surface of the *afmc* phase in the axion insulator candidate  $\text{EuIn}_2\text{As}_2$  [19] when an external in-plane field cants the magnetic moments. Similar physics can also be expected for other candidate axion insulators, such as  $\text{EuSn}_2\text{As}_2$  [29] and  $\text{EuSn}_2\text{P}_2$  [44]. With the recent rapid developments in this field, we believe that our proposed Möbius and higher-order topological phases should soon be experimentally realizable.

*Acknowledgment* - This work is supported by the Laboratory for Physical Sciences and Microsoft. R.X.Z acknowledges a JQI postdoctoral fellowship.

- 
- [1] L. Fu, Phys. Rev. Lett. **106**, 106802 (2011).  
 [2] T. H. Hsieh, H. Lin, J. Liu, W. Duan, A. Bansil, and L. Fu, Nature Communications **3**, 982 (2012).  
 [3] R. S. K. Mong, A. M. Essin, and J. E. Moore, Phys. Rev. B **81**, 245209 (2010).  
 [4] Y. Ando and L. Fu, Annual Review of Condensed Matter Physics **6**, 361 (2015).  
 [5] C.-X. Liu, R.-X. Zhang, and B. K. VanLeeuwen, Phys. Rev. B **90**, 085304 (2014).  
 [6] R.-X. Zhang and C.-X. Liu, Phys. Rev. B **91**, 115317 (2015).  
 [7] K. Shiozaki, M. Sato, and K. Gomi, Phys. Rev. B **91**, 155120 (2015).  
 [8] C. Fang and L. Fu, Phys. Rev. B **91**, 161105 (2015).  
 [9] Z. Wang, A. Alexandradinata, R. J. Cava, and B. A. Bernevig, Nature **532**, 189 EP (2016).  
 [10] P.-Y. Chang, O. Erten, and P. Coleman, Nature Physics **13**, 794 EP (2017).  
 [11] W. A. Benalcazar, B. A. Bernevig, and T. L. Hughes, Science **357**, 61 (2017).  
 [12] W. A. Benalcazar, B. A. Bernevig, and T. L. Hughes, Phys. Rev. B **96**, 245115 (2017).  
 [13] F. Schindler, A. M. Cook, M. G. Vergniory, Z. Wang, S. S. P. Parkin, B. A. Bernevig, and T. Neupert, Science Advances **4** (2018), 10.1126/sciadv.aat0346.  
 [14] J. Langbehn, Y. Peng, L. Trifunovic, F. von Oppen, and P. W. Brouwer, Phys. Rev. Lett. **119**, 246401 (2017).  
 [15] E. Khalaf, Phys. Rev. B **97**, 205136 (2018).  
 [16] E. Khalaf, H. C. Po, A. Vishwanath, and H. Watanabe, Phys. Rev. X **8**, 031070 (2018).  
 [17] F. Zhang, C. L. Kane, and E. J. Mele, Phys. Rev. Lett. **110**, 046404 (2013).  
 [18] F. Schindler, Z. Wang, M. G. Vergniory, A. M. Cook, A. Murani, S. Sengupta, A. Y. Kasumov, R. Deblock, S. Jeon, I. Drozdov, H. Bouchiat, S. Guéron, A. Yazdani, B. A. Bernevig, and T. Neupert, Nature Physics **14**, 918 (2018).  
 [19] Y. Xu, Z. Song, Z. Wang, H. Weng, and X. Dai, Phys. Rev. Lett. **122**, 256402 (2019).  
 [20] C. Yue, Y. Xu, Z. Song, H. Weng, Y.-M. Lu, C. Fang, and X. Dai, Nature Physics **15**, 577 (2019).  
 [21] Z. Wang, B. J. Wieder, J. Li, B. Yan, and B. A. Bernevig, arXiv preprint arXiv:1806.11116 (2018).  
 [22] D. Zhang, M. Shi, T. Zhu, D. Xing, H. Zhang, and J. Wang, Phys. Rev. Lett. **122**, 206401 (2019).  
 [23] M. M. Otrokov, I. I. Klimovskikh, H. Bentmann, A. Zeugner, Z. S. Aliev, S. Gass, A. U. Wolter, A. V. Koroleva, D. Estyunin, A. M. Shikin, *et al.*, (2018), arXiv:1809.07389 [cond-mat.mtrl-sci].  
 [24] Y. Gong, J. Guo, J. Li, K. Zhu, M. Liao, X. Liu, Q. Zhang, L. Gu, L. Tang, X. Feng, D. Zhang, W. Li, C. Song, L. Wang, P. Yu, X. Chen, Y. Wang, H. Yao, W. Duan, Y. Xu, S.-C. Zhang, X. Ma, Q.-K. Xue, and K. He, Chinese Physics Letters **36**, 076801 (2019).  
 [25] J. Li, Y. Li, S. Du, Z. Wang, B.-L. Gu, S.-C. Zhang, K. He, W. Duan, and Y. Xu, Science Advances **5** (2019), 10.1126/sciadv.aaw5685.  
 [26] R. C. Vidal, H. Bentmann, T. R. F. Peixoto, A. Zeugner, S. Moser, C.-H. Min, S. Schatz, K. Kifner, M. Ünzelmann, C. I. Fornari, H. B. Vasili, M. Valvidares, K. Sakamoto, D. Mondal, J. Fujii, I. Vobornik, S. Jung, C. Cacho, T. K. Kim, R. J. Koch, C. Jozwiak, A. Bostwick, J. D. Denlinger, E. Rotenberg, J. Buck, M. Hoesch, F. Diekmann, S. Rohlf, M. Kalläne, K. Rossnagel, M. M. Otrokov, E. V. Chulkov, M. Ruck, A. Isaeva, and F. Reinert, Phys. Rev. B **100**, 121104 (2019).  
 [27] C. Hu, X. Zhou, P. Liu, J. Liu, P. Hao, E. Emmanouilidou, H. Sun, Y. Liu, H. Bräwer, A. P. Ramirez, H. Cao, Q. Liu, D. Dessau, and N. Ni, (2019), arXiv:1905.02154 [cond-mat.mtrl-sci].  
 [28] J. Wu, F. Liu, M. Sasase, K. Ienaga, Y. Obata, R. Yukawa, K. Horiba, H. Kumigashira, S. Okuma, T. Inoshita, and H. Hosono, (2019), arXiv:1905.02385 [cond-mat.mtrl-sci].  
 [29] H. Li, S.-Y. Gao, S.-F. Duan, Y.-F. Xu, K.-J. Zhu, S.-J. Tian, W.-H. Fan, Z.-C. Rao, J.-R. Huang, J.-J. Li, *et al.*, (2019), arXiv:1907.06491 [cond-mat.mtrl-sci].  
 [30] Y.-J. Hao, P. Liu, Y. Feng, X.-M. Ma, E. F. Schwier, M. Arita, S. Kumar, C. Hu, R. Lu, M. Zeng, *et al.*, (2019), arXiv:1907.03722 [cond-mat.mtrl-sci].  
 [31] Y. Chen, L. Xu, J. Li, Y. Li, C. Zhang, H. Li, Y. Wu, A. Liang, C. Chen, S. Jung, *et al.*, (2019), arXiv:1907.05119 [cond-mat.mtrl-sci].  
 [32] R. C. Vidal, A. Zeugner, J. I. Facio, R. Ray, M. H. Haghighi, A. U. Wolter, L. T. C. Bohorquez, F. Caglieris, S. Moser, T. Figgemeier, *et al.*, (2019), arXiv:1906.08394 [cond-mat.mtrl-sci].  
 [33] M. Z. Shi, B. Lei, C. S. Zhu, D. H. Ma, J. H. Cui, Z. L. Sun, J. J. Ying, and X. H. Chen, (2019), arXiv:1910.08912 [cond-mat.mtrl-sci].  
 [34] L. Ding, C. Hu, F. Ye, E. Feng, N. Ni, and H. Cao, (2019), arXiv:1910.06248 [cond-mat.str-el].

- [35] S. Tian, S. Gao, S. Nie, Y. Qian, C. Gong, Y. Fu, H. Li, W. Fan, P. Zhang, T. Kondo, S. Shin, J. Adell, H. Fedderwitz, H. Ding, Z. Wang, T. Qian, and H. Lei, (2019), arXiv:1910.10101 [cond-mat.mtrl-sci].
- [36] L. X. Xu, Y. H. Mao, H. Y. Wang, J. H. Li, Y. J. Chen, Y. Y. Y. Xia, Y. W. Li, J. Zhang, H. J. Zheng, K. Huang, C. F. Zhang, S. T. Cui, A. J. Liang, W. Xia, H. Su, S. W. Jung, C. Cacho, M. X. Wang, G. Li, Y. Xu, Y. F. Guo, L. X. Yang, Z. K. Liu, and Y. L. Chen, (2019), arXiv:1910.11014 [cond-mat.mtrl-sci].
- [37] Y. Hu, L. Xu, M. Shi, A. Luo, S. Peng, Z. Y. Wang, J. J. Ying, T. Wu, Z. K. Liu, C. F. Zhang, Y. L. Chen, G. Xu, X. H. Chen, and J. F. He, (2019), arXiv:1910.11323 [cond-mat.mtrl-sci].
- [38] Y. Deng, Y. Yu, M. Z. Shi, J. Wang, X. H. Chen, and Y. Zhang, (2019), arXiv:1904.11468 [cond-mat.mtrl-sci].
- [39] J. Ge, Y. Liu, J. Li, H. Li, T. Luo, Y. Wu, Y. Xu, and J. Wang, (2019), arXiv:1907.09947 [cond-mat.mes-hall].
- [40] C. Liu, Y. Wang, H. Li, Y. Wu, Y. Li, J. Li, K. He, Y. Xu, J. Zhang, and Y. Wang, (2019), arXiv:1905.00715 [cond-mat.mes-hall].
- [41] C.-X. Liu, X.-L. Qi, H. Zhang, X. Dai, Z. Fang, and S.-C. Zhang, Phys. Rev. B **82**, 045122 (2010).
- [42] A. M. Turner, Y. Zhang, R. S. K. Mong, and A. Vishwanath, Phys. Rev. B **85**, 165120 (2012).
- [43] H. Kim, K. Shiozaki, and S. Murakami, Phys. Rev. B **100**, 165202 (2019).
- [44] X. Gui, I. Pletikosic, H. Cao, H.-J. Tien, X. Xu, R. Zhong, G. Wang, T.-R. Chang, S. Jia, T. Valla, W. Xie, and R. J. Cava, (2019), arXiv:1903.03888 [cond-mat.mtrl-sci].